

Implicit High-Order Gas Kinetic Scheme for Turbulence Simulation

G. Y. Cao*, K. Xu*, H. M. Su**
Corresponding author: makxu@ust.hk

* Hong Kong University of Science and Technology, Clear Water Bay, Kowloon, Hong Kong.

** National Key Laboratory of Science and Technology on Aerodynamic Design and Research, Northwestern Polytechnical University, Xi'an, Shaanxi, China.

Abstract: In recent years, coupled with the Reynolds averaged Navier-Stokes (RANS) models, the large eddy simulation (LES) models, and the hybrid RANS/LES models, the second-order gas-kinetic scheme (GKS) has been used in the turbulent flow simulations. At the same time, high-order GKS has been developed, such as the two-stage fourth-order scheme (S2O4), and used for laminar flow calculations. The S2O4 GKS achieves fourth-order accuracy in space and time and shows distinguishable robustness for the discontinuous flows. In this paper, targeting on the three-dimensional turbulent flows, an implicit high-order GKS with Lower-Upper Symmetric Gauss-Seidel (LU-SGS) technique is developed under the S2O4 framework. Based on Vreman-type LES model and $k - \omega$ SST model, a turbulent relaxation time is obtained and used for an enlarged particle collision time in the implicit high-order GKS in the high-Reynolds number turbulent flows. Numerical experiments include Taylor-Green vortex problem, incompressible decaying homogeneous isotropic turbulence, incompressible high-Reynolds number flat plate turbulent flow, and transonic high-Reynolds number ARA M100 wing-body flow. Comparisons among the numerical solutions from current implicit high-order GKS, the explicit high-order GKS, the second-order GKS, the second-order Navier-Stokes solver, and experimental measurements, have been conducted. Through these example, it is concluded that the current scheme has high accuracy in space and time, and significant acceleration on computational efficiency, as well as super robustness in simulating complex flows. This study also indicates that turbulence modeling plays a dominant role in the capturing physical solution. For example, the possible error in turbulent models can become the leading error in a numerical simulation, such as in the transonic three-dimensional complex RANS simulation, in comparison with numerical discretization errors. So, the development of appropriate turbulence models is still the dominant task in turbulence simulation.

Keywords: Implicit high-order GKS, LU-SGS, Two-stage fourth-order scheme, Computational efficiency, Time-relaxation turbulence simulation.

1 Introduction

Turbulence is an important research object among physics, applied mathematics, and engineering applications [1]. Because of its multi-scale features in space and time, it is a challenge to properly balance the accuracy requirements and computational costs [2] in the simulations, especially for high-Reynolds number turbulent flows. Currently, there are mainly four approaches for turbulence simulation, namely direct numerical simulation (DNS), LES, RANS, and hybrid RANS/LES methods.

Theoretically, DNS is supposed to resolve turbulent structures above the Kolmogorov dissipation scale by grid and time step resolution, but the prohibitive cost limits DNS's engineering applications. In order to study turbulent flow on unresolved grids, such as for the high-Reynolds number turbulence problems, the RANS models [3], the LES models [4], and the hybrid RANS/LES methods [5, 6] have been developed.

RANS captures turbulent structures above integral scale under the constraints of computational resources, which has been widely used in engineering turbulence simulations. LES solves the filtered Navier-Stokes equations with resolvable turbulent structures above the inertial scale. Even though LES is quite expensive compared with RANS, for unsteady separation turbulent flows, LES has gradually become an indispensable tool to obtain high-resolution turbulent flow fields. To combine the advantages of RANS and LES, the hybrid RANS/LES methods have been proposed and become hot topics in turbulence simulations, which keep good balance between resolution accuracy and computational cost.

In the past decades, the second-order GKS [7, 8] based on the Bhatnagar-Gross-Krook (BGK) [9] model has achieved great success for laminar flow computations from incompressible low-speed flow to hypersonic one. It has been extended to flows with multi-temperature [10], gravity field [11], and magnetohydrodynamics [12]. For turbulent flows, GKS can be directly used as a DNS for low-Reynolds number flow [13, 14]. The "mixing time" was proposed for kinetic equation based methods for high-Reynolds number turbulence [15, 16], which can be regarded as an extension of BGK model with a newly defined collision (relaxation) time τ_t . Following this "mixing time" concept, the second-order gas kinetic schemes coupled with S-A model [17], $k - \omega$ SST model [18, 19, 20], Vreman-type LES model, and the hybrid RANS/LES methods [21] have been developed and implemented in high-Reynolds number turbulent flow simulations. Most previous work are based on the explicit second-order GKS coupled with traditional turbulence models. In view of the high-resolution requirement for turbulence simulation, it is fully legitimate to construct high-order GKS coupled with traditional turbulence models.

In recent years, an accurate and robust S2O4 GKS [22, 23, 24] has been developed for laminar flows, which achieves fourth-order accuracy in space and time and shows high efficiency and robustness in the flow simulations with shocks. Focusing on the extension of the scheme to the three-dimensional turbulent flows, an implicit high-order GKS is proposed in this paper. On the one hand, the S2O4 GKS framework is used to provide a solid foundation for obtaining high-resolution flow fields in turbulent flow. On the other hand, LU-SGS method [25, 26] is implemented to overcome the time step barrier in the explicit scheme, and makes the CFL number large in the three-dimensional high-Reynolds turbulent flows. In what follows, Section 2 presents the construction of this implicit high-order GKS under two-stage fourth-order framework. This is followed by the coupling of Vreman-type LES model [27] and the $k - \omega$ SST [28] model in the current implicit high-order GKS in Section 3. The numerical simulations from incompressible low-speed to transonic three-dimensional complex turbulent flows will be presented in section 4. And the final section is the conclusion and discussion.

2 Implicit three-dimensional two-stage fourth-order GKS solver

2.1 Three-dimensional finite volume framework based on BGK model

Based on particle transport and collision, the Boltzmann equation has been constructed for monotonic dilute gas. The simplification of the Boltzmann equation given by the BGK model has the following form [9],

$$\frac{\partial f}{\partial t} + u \frac{\partial f}{\partial x} + v \frac{\partial f}{\partial y} + w \frac{\partial f}{\partial z} = \frac{g - f}{\tau}, \quad (1)$$

where f is the number density of molecules at position (x, y, z) and particle velocity (u, v, w) at time t . The left side of the Eq.(1) denotes the free transport term, and the right hand side represents the collision term. The relation between distribution function f and macroscopic variables, such as mass, momentum, energy and stress, can be obtained by taking moments in velocity of the gas distribution function. The collision operator in BGK model shows simple relaxation process from f to a local equilibrium state g , with a characteristic time scale τ , which is related to the viscosity and heat conduction coefficients. The local equilibrium state is a Maxwellian distribution,

$$g = \rho \left(\frac{\lambda}{\pi}\right)^{\frac{\kappa+3}{2}} e^{-\lambda[(u-U)^2 + (v-V)^2 + (w-W)^2 + \xi^2]}, \quad (2)$$

where ρ is the density, (U, V, W) are the macroscopic fluid velocity in the x -, y - and z - directions. Here $\lambda = m/2kT$, m is the molecular mass, k is the Boltzmann constant, and T is the temperature. For three-

dimensional equilibrium diatomic gas, the total number of degrees of freedom in ξ is $K = 2$, which accounts for the two rotational modes $\xi^2 = \xi_1^2 + \xi_2^2$, and the specific heat ratio $\gamma = (K + 5)/(K + 3)$ is determined.

The relation between mass ρ , momentum($\rho U, \rho V, \rho W$), total energy ρE with the distribution function f is given by,

$$W = \begin{pmatrix} \rho \\ \rho U \\ \rho V \\ \rho W \\ \rho E \end{pmatrix} = \int \psi_\alpha f d\Xi, \quad \alpha = 1, 2, 3, 4, 5, \quad (3)$$

where $d\Xi = dudvdwd\xi_1d\xi_2$ and ψ_α is the component of the vector of collision invariants

$$\psi = (\psi_1, \psi_2, \psi_3, \psi_4, \psi_5)^T = (1, u, v, w, \frac{1}{2}(u^2 + v^2 + w^2 + \xi^2))^T.$$

Since only mass, momentum and total energy are conserved during particle collisions, the compatibility condition for the collision term turns into,

$$\int \frac{g - f}{\tau} \psi d\Xi = 0, \quad (4)$$

at any point in space and time.

Based on the above BGK model as Eq.(1), the Euler equations can be obtained for a local equilibrium state with $f = g$. On the other hand, the Navier-Stokes equations, the stress and Fourier heat conduction terms can be derived with the Chapman-Enskog expansion [29] truncated to the 1st-order of τ ,

$$f = g + Knf_1 = g - \tau \left(\frac{\partial g}{\partial t} + u \frac{\partial g}{\partial x} + v \frac{\partial g}{\partial y} + w \frac{\partial g}{\partial z} \right). \quad (5)$$

For the Burnett and super-Burnett solutions, the above expansion can be naturally extended [30], such as $f = g + Knf_1 + Kn^2f_2 + Kn^3f_3 + \dots$. For the above Navier-Stokes solutions, the GKS based on the kinetic BGK model has been well developed [7]. In order to simulate the flow with any realistic Prandtl number, a modification of the heat flux in the energy transport is used in this scheme, which is also implemented in the present study.

Taking moments of Eq.(1) and integrating over the control volume $V_{ijk} = \bar{x}_i \times \bar{y}_j \times \bar{z}_k$ with $\bar{x}_i = [x_i - \frac{\Delta x}{2}, x_i + \frac{\Delta x}{2}]$, $\bar{y}_j = [y_j - \frac{\Delta y}{2}, y_j + \frac{\Delta y}{2}]$, $\bar{z}_k = [z_k - \frac{\Delta z}{2}, z_k + \frac{\Delta z}{2}]$, the three-dimensional finite volume scheme can be written as

$$\begin{aligned} \frac{dW_{ijk}}{dt} = L(W_{ijk}) = & \frac{1}{|V_{ijk}|} \left[\int_{\bar{y}_j \times \bar{z}_k} (F_{i-1/2,j,k} - F_{i+1/2,j,k}) dydz \right. \\ & \left. + \int_{\bar{x}_i \times \bar{z}_k} (G_{i,j-1/2,k} - G_{i,j+1/2,k}) dx dz + \int_{\bar{x}_i \times \bar{y}_j} (H_{i,j,k-1/2} - G_{i,j,k+1/2}) dx dy \right], \end{aligned} \quad (6)$$

where W_{ijk} are the cell averaged conservative variables mass, momentum and total energy. All of them are averaged over control volume V_{ijk} and volume of the numerical cell is $|V_{ijk}| = \Delta x \Delta y \Delta z$. Here, numerical fluxes in x - direction is presented as an example

$$\int_{\bar{y}_j \times \bar{z}_k} F_{i+1/2,j,k} dydz = F_{\mathbf{x}_{i+1/2,j,k},t} \Delta y \Delta z. \quad (7)$$

Based on the fifth-order WENO-JS spatial reconstruction on the primitive flow variables [31], the reconstructed point value and the spatial derivatives in normal and tangential direction can be obtained. In the smooth flow computation, the linear form of WENO-JS is adopted to reduce the dissipation. To save computational resources for three-dimensional large-scale problems, Gaussian points have not been used in this study. For three-dimensional The numerical fluxes $F_{\mathbf{x}_{i+1/2,j,k},t}$ can be provided by the flow solvers,

which can be evaluated by taking moments of the gas distribution function as

$$F_{\mathbf{x}_{i+1/2,j,k},t} = \int \psi_\alpha u f(\mathbf{x}_{i+1/2,j,k}, t, \mathbf{u}, \xi) d\Xi, \quad \alpha = 1, 2, 3, 4, 5. \quad (8)$$

Here $f(\mathbf{x}_{i+1/2,j,k}, t, \mathbf{u}, \xi)$ is based on the integral solution of BGK equation Eq.(1) at the cell interface

$$f(\mathbf{x}_{i+1/2,j,k}, t, \mathbf{u}, \xi_r) = \frac{1}{\tau} \int_0^t g(\mathbf{x}', t', \mathbf{u}, \xi_r) e^{-(t-t')/\tau} dt' + e^{-t/\tau} f_0(-\mathbf{u}t, \xi_r), \quad (9)$$

where $\mathbf{x}_{i+1/2,j,k} = \mathbf{0}$ is the location of cell interface, $\mathbf{u} = (u, v, w)$ is the particle velocity, $\mathbf{x}_{i+1/2,j,k} = \mathbf{x}' + \mathbf{u}(t - t')$ is the trajectory of particles. f_0 is the initial gas distribution, and g is the corresponding intermediate equilibrium state as Eq.(2). g and f_0 can be constructed as

$$g = g_0(1 + \bar{a}x + \bar{b}y + \bar{c}z + \bar{A}t),$$

and

$$f_0 = \begin{cases} g_l[1 + (a_l x + b_l y + c_l z) - \tau(a_l u + b_l v + c_l w + A_l)], & x \leq 0 \\ g_r[1 + (a_r x + b_r y + c_r z) - \tau(a_r u + b_r v + c_r w + A_r)], & x > 0, \end{cases}$$

where g_l and g_r are the initial gas distribution functions on both sides of a cell interface. g_0 is the initial intermediate equilibrium state located at cell interface, which can be determined through the compatibility condition

$$\int \psi_\alpha g_0 d\Xi = \int_{u>0} \psi_\alpha g_l d\Xi + \int_{u<0} \psi_\alpha g_r d\Xi, \quad \alpha = 1, 2, 3, 4, 5.$$

For the second-order flux, the time-dependent gas distribution function at cell interfaces is evaluated as

$$\begin{aligned} f(\mathbf{x}_{i+1/2,j,k}, t, \mathbf{u}, \xi_r) &= (1 - e^{-t/\tau})g_0 + ((t + \tau)e^{-t\tau} - \tau)(\bar{a}u + \bar{b}v + \bar{c}w)g_0 \\ &\quad + (t - \tau + \tau e^{-t\tau})\bar{A}g_0 \\ &\quad + e^{-t/\tau}g_l[1 - (\tau + t)(a_l u + b_l v + c_l w) - \tau A_l](1 - H(u)) \\ &\quad + e^{-t/\tau}g_r[1 - (\tau + t)(a_r u + b_r v + c_r w) - \tau A_r]H(u), \end{aligned} \quad (10)$$

where the coefficients in Eq.(10) can be determined by the spatial derivatives of macroscopic flow variables and the compatibility condition as the Appendix C in [8].

Here, the second-order accuracy in time can be achieved by one step integration, with the second-order gas-kinetic solver Eq.(10). Based on a high-order expansion of the equilibrium state around a cell interface, the one-stage high-order GKS has been developed successfully [32, 33, 34]. However, the one-stage gas-kinetic solver become very complicated, especially for three-dimensional multidimensional computations.

2.2 Two-stage high-order temporal discretization

In recent study, a two-stage fourth-order time-accurate discretization was developed for Lax-Wendroff flow solvers, particularly applied for hyperbolic equations with the generalized Riemann problem(GRP) solver [22] and the GKS [23]. Such method provides a reliable framework to develop the implicit three-dimensional high-order GKS with a second-order flux function Eq.(10). The key point for this two-stage fourth-order method is to use time derivative of flux function. In order to obtain the time derivative of flux function at t^n and $t^* = t_n + \Delta t/2$, the flux function should be approximated as a linear function of time within a time interval.

According to the numerical fluxes at cell interface Eq.(8), the following notation is introduced

$$\mathbb{F}_{i+1/2,j,k}(W^n, \delta) = \int_{t_n}^{t_n+\delta} \mathbf{F}_{i+1/2,j,k}(W^n, t) dt = \int_{t_n}^{t_n+\delta} F_{\mathbf{x}_{i+1/2,j,k},t} dt. \quad (11)$$

In the time interval $[t_n, t_n + \Delta t/2]$, the flux is expanded as the following linear form

$$\mathbf{F}_{i+1/2,j,k}(W^n, t) = \mathbf{F}_{i+1/2,j,k}^n + \partial_t \mathbf{F}_{i+1/2,j,k}^n (t - t_n). \quad (12)$$

Based on Eq.(11) and linear expansion of flux as Eq.(12), the coefficients $\mathbf{F}_{i+1/2,j,k}(W^n, t_n)$ and $\partial_t \mathbf{F}_{i+1/2,j,k}(W^n, t_n)$ can be determined as,

$$\begin{aligned} \mathbf{F}_{i+1/2,j,k}(W^n, t_n) \Delta t + \frac{1}{2} \partial_t \mathbf{F}_{i+1/2,j,k}(W^n, t_n) \Delta t^2 &= \mathbb{F}_{i+1/2,j,k}(W^n, \Delta t), \\ \frac{1}{2} \mathbf{F}_{i+1/2,j,k}(W^n, t_n) \Delta t + \frac{1}{8} \partial_t \mathbf{F}_{i+1/2,j,k}(W^n, t_n) \Delta t^2 &= \mathbb{F}_{i+1/2,j,k}(W^n, \Delta t/2). \end{aligned}$$

By solving the linear system, we have

$$\begin{aligned} \mathbf{F}_{i+1/2,j,k}(W^n, t_n) &= (4\mathbb{F}_{i+1/2,j,k}(W^n, \Delta t/2) - \mathbb{F}_{i+1/2,j,k}(W^n, \Delta t))/\Delta t, \\ \partial_t \mathbf{F}_{i+1/2,j,k}(W^n, t_n) &= 4(\mathbb{F}_{i+1/2,j,k}(W^n, \Delta t) - \mathbb{F}_{i+1/2,j,k}(W^n, \Delta t/2))/\Delta t^2, \end{aligned} \quad (13)$$

and $\mathbf{F}_{i+1/2,j,k}(W^*, t_*)$, $\partial_t \mathbf{F}_{i+1/2,j,k}(W^*, t_*)$ for the intermediate state t_* can be constructed similarly.

With these notations, the high-order algorithm for three-dimensional flow is given by the following steps.

(i) With the initial reconstruction, update W^* at $t_* = t_n + \Delta t/2$ by

$$\begin{aligned} W_{ijk}^* &= W_{ijk}^n - \frac{1}{\Delta x} [\mathbb{F}_{i+1/2,j,k}(W^n, \Delta t/2) - \mathbb{F}_{i-1/2,j,k}(W^n, \Delta t/2)] \\ &\quad - \frac{1}{\Delta y} [\mathbb{G}_{i,j+1/2,k}(W^n, \Delta t/2) - \mathbb{G}_{i,j-1/2,k}(W^n, \Delta t/2)] \\ &\quad - \frac{1}{\Delta z} [\mathbb{H}_{i,j,k+1/2}(W^n, \Delta t/2) - \mathbb{H}_{i,j,k-1/2}(W^n, \Delta t/2)], \end{aligned} \quad (14)$$

and compute the fluxes and their derivatives by Eq.(13) for future using,

$$\begin{aligned} \mathbf{F}_{i+1/2,j,k}(W^n, t_n), \mathbf{G}_{i,j+1/2,k}(W^n, t_n), \mathbf{H}_{i,j,k+1/2}(W^n, t_n), \\ \partial_t \mathbf{F}_{i+1/2,j,k}(W^n, t_n), \partial_t \mathbf{G}_{i,j+1/2,k}(W^n, t_n), \partial_t \mathbf{H}_{i,j,k+1/2}(W^n, t_n). \end{aligned}$$

(ii) Reconstruct intermediate value W_{ijk}^* and compute

$$\partial_t \mathbf{F}_{i+1/2,j,k}(W^*, t_*), \partial_t \mathbf{G}_{i,j+1/2,k}(W^*, t_*), \partial_t \mathbf{H}_{i,j,k+1/2}(W^*, t_*),$$

where the derivatives are determined by Eq.(13) in the time interval $[t_*, t_* + \Delta t]$.

(iii) Update W_{ijk}^{n+1} by

$$\begin{aligned} W_{ijk}^{n+1} &= W_{ijk}^n - \frac{\Delta t}{\Delta x} [\mathcal{F}_{i+1/2,j,k}^n - \mathcal{F}_{i-1/2,j,k}^n] \\ &\quad - \frac{\Delta t}{\Delta y} [\mathcal{G}_{i,j+1/2,k}^n - \mathcal{G}_{i,j-1/2,k}^n] - \frac{\Delta t}{\Delta z} [\mathcal{H}_{i,j,k+1/2}^n - \mathcal{H}_{i,j,k-1/2}^n], \end{aligned} \quad (15)$$

where $\mathcal{F}_{i+1/2,j,k}^n$, $\mathcal{G}_{i,j+1/2,k}^n$ and $\mathcal{H}_{i,j,k+1/2}^n$ are the numerical fluxes and expressed as

$$\begin{aligned} \mathcal{F}_{i+1/2,j,k}^n &= \mathbf{F}_{i+1/2,j,k}(W^n, t_n) + \frac{\Delta t}{6} [\partial_t \mathbf{F}_{i+1/2,j,k}(W^n, t_n) + 2\partial_t \mathbf{F}_{i+1/2,j,k}(W^*, t_*)], \\ \mathcal{G}_{i,j+1/2,k}^n &= \mathbf{G}_{i,j+1/2,k}(W^n, t_n) + \frac{\Delta t}{6} [\partial_t \mathbf{G}_{i,j+1/2,k}(W^n, t_n) + 2\partial_t \mathbf{G}_{i,j+1/2,k}(W^*, t_*)], \\ \mathcal{H}_{i,j,k+1/2}^n &= \mathbf{H}_{i,j,k+1/2}(W^n, t_n) + \frac{\Delta t}{6} [\partial_t \mathbf{H}_{i,j,k+1/2}(W^n, t_n) + 2\partial_t \mathbf{H}_{i,j,k+1/2}(W^*, t_*)]. \end{aligned}$$

2.3 Implicit LU-SGS method

In previous work, LU-SGS method has been applied with GKS for hypersonic flows [35] and near-continuum flows [36] in two-dimensional cases. For three-dimensional flow, in order to use large CFL number to increase the computational efficiency, implicit LU-SGS method is used to update conservative variables W_{ijk}^* and W_{ijk}^{n+1} . According to Eq.(6), define the residual in the cell (i, j, k) as

$$R(W) = \overline{\Delta t}L(W),$$

where $\overline{\Delta t}$ is the time step, which is $\frac{\Delta t}{2}$ for t^* step and Δt for t^{n+1} step. The residual for t^* step and t^{n+1} step can be calculated with above explicit scheme Eq.(14) and Eq.(15), respectively. Set updating W^* as an example in the following section.

Firstly, introduce the Jacobian matrices $\mathcal{A} = \frac{\partial F}{\partial W_i}$, $\mathcal{B} = \frac{F}{\partial W_j}$, and $\mathcal{C} = \frac{F}{\partial W_k}$, with the Euler flux F for laminar flow and the extended flux when coupled with turbulence model [26]. Based on the LU-SGS technique, Eq.(14) can be written as

$$(L + D)D^{-1}(D + U)\Delta W = R(W^n), \quad (16)$$

where $\Delta W = W^* - W^n$, with

$$\begin{aligned} L &= -(\mathcal{A}_{i-1}^+ + \mathcal{B}_{j-1}^+ + \mathcal{C}_{k-1}^+), \\ D &= \frac{\mathcal{I}}{\Delta t} + \mathcal{A}_i^+ - \mathcal{A}_i^- + \mathcal{B}_j^+ - \mathcal{B}_j^- + \mathcal{C}_k^+ - \mathcal{C}_k^-, \\ U &= \mathcal{A}_{i+1}^- + \mathcal{B}_{j+1}^- + \mathcal{C}_{k+1}^-, \end{aligned}$$

and

$$\begin{aligned} \mathcal{A}^\pm &= \frac{1}{2}(\mathcal{A} \pm r_{\mathcal{A}}\mathcal{I}), r_{\mathcal{A}} = \beta\sigma_{\mathcal{A}}, \\ \mathcal{B}^\pm &= \frac{1}{2}(\mathcal{B} \pm r_{\mathcal{B}}\mathcal{I}), r_{\mathcal{B}} = \beta\sigma_{\mathcal{B}}, \\ \mathcal{C}^\pm &= \frac{1}{2}(\mathcal{C} \pm r_{\mathcal{C}}\mathcal{I}), r_{\mathcal{C}} = \beta\sigma_{\mathcal{C}}, \end{aligned}$$

where \mathcal{I} is the unit matrix, $(\sigma_{\mathcal{A}}, \sigma_{\mathcal{B}}, \sigma_{\mathcal{C}})$ are the spectral radii of the Jacobian matrices, with the coefficient $\beta \geq 1$ to ensure dominant diagonal.

Then, use two-step sweeping way to get the solution ΔW

$$\begin{aligned} (L + D)\Delta W^* &= -R(W^n), \\ (D + U)\Delta W &= D\Delta W^*. \end{aligned} \quad (17)$$

Sequently, the macroscopic flow variables are updated by

$$W^* = W^n + \Delta W. \quad (18)$$

In the similar way, Eq.(15) can be used to update the t^{n+1} step macroscopic flow variables W^{n+1} .

3 GKS coupled with turbulence model

We follow the concept of turbulent eddy viscosity, which models the effect of unresolved turbulent scales by enlarging turbulent eddy viscosity in turbulence region. Similarly, the enlarging turbulent relaxation time τ_t is proposed to describe the turbulent flows under the kinetic framework. Based on this enlarging turbulent relaxation time τ_t , extended BGK model for turbulent flows can be written as,

$$\frac{\partial f}{\partial t} + u \frac{\partial f}{\partial x} + v \frac{\partial f}{\partial y} + w \frac{\partial f}{\partial z} = \frac{g - f}{\tau + \tau_t}. \quad (19)$$

Using Chapman-Enskog expansion in [16], Eq.(19) can recover traditional RANS turbulent eddy viscosity model through the relation between turbulent eddy viscosity μ_t and turbulent relaxation time τ_t , with

$$\tau + \tau_t = \frac{\mu + \mu_t}{p}, \quad (20)$$

where p is the pressure. The key point is to get turbulent eddy viscosity μ_t , then turbulent relaxation time τ_t will be determined by Eq.(20). In [16], this enlarged relaxation time τ_t is called "mixing time", which is comparable with the classical concept of "mixing length". In this paper, based on extended BGK model and "mixing time" concept, time-relaxation turbulence simulation will be studied.

In present work, Vreman-type model for LES and $k - \omega$ SST model for RANS simulation will be used to evaluate τ_t and use the relaxation time $\tau + \tau_t$ in Eq.(19). All conserved macroscopic variables are calculated from GKS, and the turbulent viscosity is obtained from the LES/RANS eddy viscosity model. The evolution of turbulent variables depends on the conserved macroscopic variables. This coupling process is applied at each step for turbulence simulations.

3.1 LES: Vreman-type model

Smagorinsky model is the well-known eddy viscosity LES model, while it is too dissipative. With the application of a dynamic procedure, dynamic Smagorinsky model is developed to overcome the weakness of the Smagorinsky model. To keep the simple eddy viscosity closure form, Vreman-type model is proposed by Vreman in a simple algebra form, which is comparable to dynamic Smagorinsky model. For Vreman-type model, turbulent eddy viscosity μ_t is given by

$$\mu_t = \rho c \sqrt{\frac{B_\beta}{a_{ij}a_{ij}}}, \quad (21)$$

where ρ is the density, and constant $c = 2.5C_s^2$, with $C_s = 0.1$. Left unknowns in Eq.(21) can be determined through the combination of velocity gradient in resolved flowfields, as

$$\begin{cases} \alpha_{ij} &= \frac{\partial U_j}{\partial x_i}, \\ \beta_{ij} &= \Delta^2 \alpha_{mi} \alpha_{mj}, \\ B_\beta &= \beta_{11}\beta_{22} - \beta_{12}^2 + \beta_{11}\beta_{33} - \beta_{13}^2 - \beta_{22}\beta_{33} - \beta_{23}^2. \end{cases} \quad (22)$$

In Eq.(22), the U_j means the cell averaged velocity.

3.2 RANS: $k - \omega$ SST model

$k - \omega$ SST model combines the positive features of $k - \omega$ model and $k - \epsilon$ model together. For this model, evolution equation of turbulence kinetic energy k and specific dissipation rate ω are modeled as

$$\begin{aligned} \frac{\partial(\rho k)}{\partial t} + \frac{\partial}{\partial x_j} [\rho U_j k - (\mu + \sigma_k \mu_t) \frac{\partial k}{\partial x_j}] &= P - \beta^* \rho \omega k, \\ \frac{\partial(\rho \omega)}{\partial t} + \frac{\partial}{\partial x_j} [\rho u_j \omega - (\mu + \sigma_\omega \mu_t) \frac{\partial \omega}{\partial x_j}] &= \frac{\gamma}{\nu_t} P - \beta \rho \omega^2 + 2(1 - F_1) \frac{\rho \sigma_\omega}{\omega} \frac{\partial k}{\partial x_j} \frac{\partial \omega}{\partial x_j}, \end{aligned} \quad (23)$$

where P is the production of turbulence kinetic energy. In current study, P is written in SST-V2003 form, as

$$\begin{aligned} P^* &= \mu_t \Omega^2 - \frac{2}{3} \rho k \delta_{ij} \frac{\partial U_i}{\partial x_j}, \\ P &= \min(P^*, 10\beta^* \rho \omega k), \end{aligned}$$

where $\Omega = \sqrt{\Omega_{ij}\Omega_{ij}}$ is the vorticity magnitude. The turbulent eddy viscosity is computed from

$$\mu_t = \frac{\rho a_1 k}{\max\{a_1 \omega, SF_2\}}, \quad (24)$$

where $\nu_t = \mu_t/\rho$ is the turbulent kinematic viscosity, $S = \sqrt{2S_{ij}S_{ij}}$ is the shear strain rate magnitude. Ω_{ij} and S_{ij} are denoted by

$$\Omega_{ij} = \frac{1}{2}\left(\frac{\partial U_i}{\partial x_j} - \frac{\partial U_j}{\partial x_i}\right), \quad S_{ij} = \frac{1}{2}\left(\frac{\partial U_i}{\partial x_j} + \frac{\partial U_j}{\partial x_i}\right).$$

Each of the constants is a blend of an inner constant and outer constant via

$$\phi = F_1 \phi_1 + (1 - F_1) \phi_2, \quad (\phi = \sigma_k, \sigma_\omega, \beta, \gamma)$$

where ϕ_1 represents the inner constants of $k - \omega$ model and ϕ_2 represents the outer constants of the $k - \epsilon$ model. For inner layer,

$$\sigma_{k1} = 0.85, \quad \sigma_{\omega1} = 0.5, \quad \beta_1 = 0.075, \quad \gamma_1 = \frac{5}{9},$$

and for outer layer,

$$\sigma_{k2} = 1.0, \quad \sigma_{\omega2} = 0.856, \quad \beta_2 = 0.0828, \quad \gamma_2 = 0.44.$$

F_1 and F_2 are hybrid functions are given by

$$F_1 = \tanh\left\{\min\left[\max\left(\frac{\sqrt{k}}{\beta^* \omega d}, \frac{500\mu}{\rho \omega d^2}\right), \frac{4\rho\sigma_{\omega2}k}{CD_{k\omega}d^2}\right]\right\}^4,$$

$$F_2 = \tanh\left[\max\left(\frac{2\sqrt{k}}{0.09\omega d}, \frac{500\mu}{\rho \omega d^2}\right)\right]^2,$$

$$CD_{k\omega} = \max\left(\frac{2\rho\sigma_{\omega2}}{\omega} \frac{\partial k}{\partial x_j} \frac{\partial \omega}{\partial x_j}, 10^{-10}\right),$$

where d is the coldest distance from the field point to the nearest wall, and left constants are $a_1 = 0.31$ and $\beta^* = 0.09$.

In this paper, turbulent variables k and ω are updated separately from the conservative variables in the GKS. Incorporated with second-order GKS solutions for conservative flow variables, the turbulent equations are solved with van Leer limiter and Roe scheme for advection terms, and second-order center difference for source terms. When coupled with the high-order GKS solutions, the turbulent models are solved by WENO-JS reconstruction and Roe scheme for advection terms and fourth-order center difference for source terms.

4 Numerical tests

In this section, numerical tests from low-speed smooth flow to transonic flow will be presented to validate our numerical scheme. The collision time τ takes

$$\tau = \frac{\mu}{p} + C \frac{|p_l - p_r|}{|p_l + p_r|} \Delta t,$$

where μ is the viscous coefficient obtained from Sutherland's Law, and C is set to be 1.5 in the computation. p_l and p_r denote the pressures on the left and right sides at the cell interface. In smooth flow region, τ goes to $\tau = \mu/p$ automatically. Δt is the time step which is determined according to the CFL condition.

4.1 DNS 3D case: Taylor-Green vortex

Taylor-Green vortex is a benchmark to validate the performance of high-order scheme. Here, the explicit high-order GKS is performed on this case for verifying the high-order accuracy in space and time. With a uniform temperature field, the initial condition is given by

$$\begin{aligned} U &= V_0 \sin\left(\frac{x}{L}\right) \cos\left(\frac{y}{L}\right) \cos\left(\frac{z}{L}\right), \\ V &= -V_0 \cos\left(\frac{x}{L}\right) \sin\left(\frac{y}{L}\right) \cos\left(\frac{z}{L}\right), \\ W &= 0, \\ p &= p_0 + \frac{\rho_0 V_0^2}{16} \left(\cos\left(\frac{2x}{L}\right) + \cos\left(\frac{2y}{L}\right) \right) \left(\cos\left(\frac{2z}{L}\right) + 2 \right). \end{aligned}$$

The fluid is a perfect gas with $\gamma = 1.4$ and the Prandtl number is $Pr = 0.71$. The flow is computed within a periodic square box defined as $-\pi L \leq x, y, z \leq \pi L$. The characteristic convective time $t_c = L/V_0$. In the computation, $L = 1$, $V_0 = 1$, $\rho_0 = 1$, and the Mach number takes $M_0 = V_0/c_0 = 0.1$ and Reynolds number $Re = 280$, where c_0 is the sound speed.

The volume-averaged kinetic energy can be computed from the flow as it evolves in time, which is expressed as

$$E_k = \frac{1}{\rho_0 \Omega} \int_{\Omega} \frac{1}{2} \rho \mathbf{U} \cdot \mathbf{U} d\Omega,$$

where Ω is the volume of the computational domain, and the dissipation rate of the kinetic energy is given by

$$\epsilon_k = -\frac{dE_k}{dt}.$$

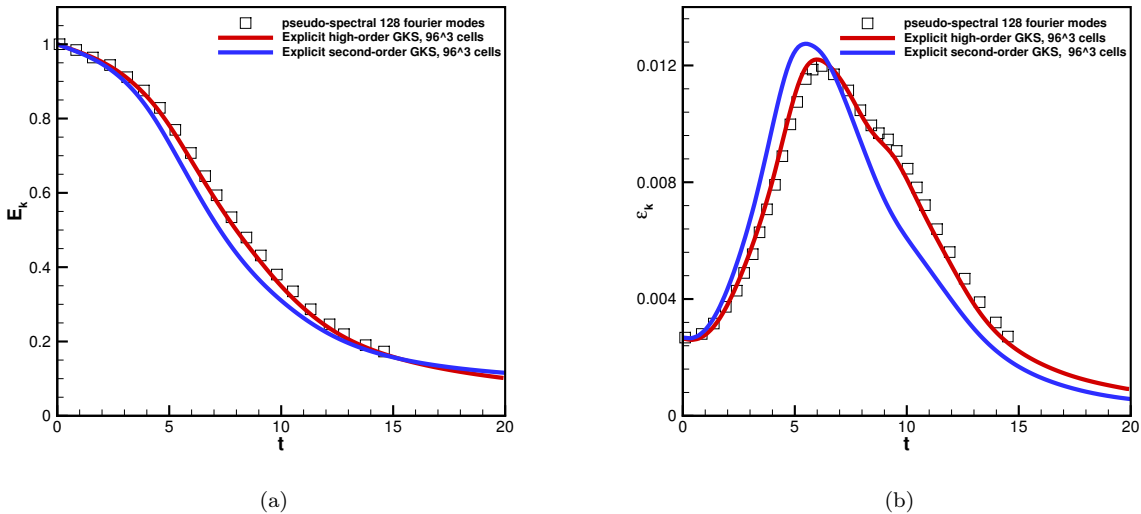


Figure 1: The volume-averaged kinetic energy E_k (a) and the dissipation rate ϵ_k (b) based on the explicit high-order GKS and the explicit second-order GKS.

With $96 \times 96 \times 96$ mesh points, DNS is implemented based on the explicit high-order GKS. The numerical result of the explicit high-order scheme and the explicit second-order scheme for the normalized volume-averaged kinetic energy and dissipation rate are presented in Figure 1. Compared with the DNS results from pseudo-spectral method [37], the explicit high-order GKS outweighs the explicit second-order GKS

obviously. The explicit high-order GKS has a close match with the pseudo-spectral result, while the explicit second-order GKS has a larger dissipation rate when $t \leq 7$ as well as the incorrect behavior after this. This Taylor-Green vortex problem provides the validation for the high-order accuracy in space and time of the current high-order GKS. At each cell interface, only the central point is used for the flux evaluation in the high-order GKS.

4.2 LES 3D case: homogeneous isotropic turbulence in incompressible flow

Incompressible decaying homogeneous isotropic turbulence (IDHIT) is the most fundamental problem for turbulence theory and model validation, especially for LES model. In current study, the reference experiment is conducted by Comte-Bellot et al. [38], with Taylor Reynolds number $Re_\lambda = 71.6$ and turbulent Mach number $Ma_t = 0.2$. Here, computation domain is a $(2\pi)^3$ box with $64 \times 64 \times 64$ or $128 \times 128 \times 128$ uniform grids, and Vreman-type LES model is used with periodic boundary condition in 6 faces.

The turbulent fluctuating velocity u' , the Taylor microscale λ , the Taylor Reynolds number Re_λ , the turbulent Mach number Ma_t , and the spectral of turbulence kinetic energy (TKE) are defined as

$$\begin{aligned}
 u' &= \langle (u_1^2 + u_2^2 + u_3^2)/3 \rangle^{1/2}, \\
 \lambda^2 &= \frac{u'^2}{\langle (\partial u_1 / \partial x_1)^2 \rangle}, \\
 Re_\lambda &= \frac{u' \lambda}{\nu}, \\
 Ma_t &= \frac{\langle u_1^2 + u_2^2 + u_3^2 \rangle^{1/2}}{c}, \\
 E(\kappa) &= \frac{1}{2} \int_{\kappa_{min}}^{\kappa_{max}} \Phi_{ii}(\boldsymbol{\kappa}) \delta(|\boldsymbol{\kappa}| - \kappa) d\boldsymbol{\kappa},
 \end{aligned}$$

where $\langle \dots \rangle$ represents the space average in computation domain. c represents the local sound speed, and ν represents the kinematic viscosity as μ/ρ . Velocity spectral Φ_{ii} is the Fourier transform of two-point correlation, with wave number $\kappa_{min} = 0$ and $\kappa_{max} = 64$. The initial velocity fields is computed from experiment energy spectral, with constant pressure, density and temperature.

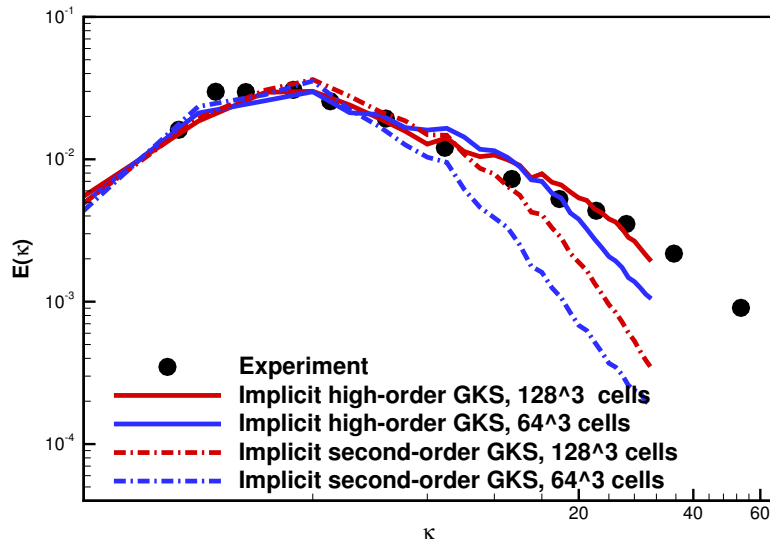


Figure 2: Spectral of TKE at dimensionless time $t^* = 0.87$ based on the implicit high-order GKS and the implicit second-order GKS.

LES calculations with the implicit high-order GKS and implicit second-order GKS on $64 \times 64 \times 64$ and $128 \times 128 \times 128$ mesh points are performed. Figure 2 shows the spectral of TKE at dimensionless time $t^* = 0.87$, based on the implicit high-order GKS and the implicit second-order GKS. Spectral of TKE based on the explicit scheme almost has no difference with the implicit scheme, so they have not been shown in here. With the same grid, in high wavenumber region, TKE spectral from the implicit high-order scheme is much closer to the experiment result, which outweighs results from the implicit second-order scheme. In particular, result of the high-order scheme on $64 \times 64 \times 64$ mesh points performs better than that of the second-order scheme on $128 \times 128 \times 128$ mesh points. This shows that high-order accuracy solutions in space and time are obtained in this IDHIT system with the Vreman-type LES model. In addition, for implicit scheme, the CFL number can reach 1.5 maximally, while the maximum CFL number is 0.32 for the explicit scheme. So, a large CFL number has been obtained in this implicit scheme.

4.3 RANS 2D case: incompressible flow with zero pressure gradient over a flat plate

Two-dimensional zero pressure gradient smooth flow over flat plate is used to test the high efficiency of the implicit high-order GKS. Free stream condition is Mach number $Ma = 0.2$, and Reynolds number $Re = 5 \times 10^6$ with reference length 1.0. The computation domain includes the length of the flat plate $L = 2.0$, the height of the flow field $H = 1.0$, and the leading edge of the flat plate at $x = 0$. Boundary conditions are imposed as the reference data in the website [39]. As presented in table 1, the second-order GKS and CFL3D are implemented on fine G2 grid, while the high-order GKS is performed on moderate G1 grid. The total grid of G2 is almost 4 times larger than that of G1, and a smaller Y^+ is used in G2. Here, Y^+ is the non-dimensional wall distance for the first level grid upon the wall.

Table 1: Grid information of moderate G1 grid and fine G2 grid

Grid	$N_x \times N_y$	Total grid	Y^+	Solver
G1	273×193	52689	0.2	high-order GKS
G2	543×385	209825	0.08	second-order GKS/CFL3D

G1 grid is split into 5 blocks for parallel computing on Intel Xeon E5-2962 v2 cores provided by TianHe-II in Guangzhou. As table 2 presents, maximum CFL number for the implicit high-order GKS is 3.0. However the maximum CFL number for explicit high-order GKS is 0.2. On moderate G1 grid, considering the CPU time/each step for the two schemes, the implicit high-order GKS can speed up 13.6 times than the explicit high-order GKS. Residual convergence curves of these two schemes are plotted in Figure 3. Table 2 also shows the implicit high-order GKS on moderate G1 grid, which is 1.5 times faster than the implicit second-order GKS on fine G2 grid for the same residual decrease as shown in Figure 3. Furthermore, Figure 3 shows the total residual decreasing from the implicit high-order GKS on moderate G1 grid is larger than that of the implicit second-order GKS on fine G2 grid.

Table 2: Maximum CFL number and CPU time for the implicit/explicit high-order GKS on G1 grid and the implicit second-order GKS on G2 grid

Numerical scheme	Grid	Max CFL number	CPU time
Implicit high-order GKS	G1	3.0	0.56 s /each step
Explicit high-order GKS	G1	0.2	0.51 s /each step
Implicit second-order GKS	G2	3.2	1.55 s /each step

Total residuals of all cases reduce down to the 5 orders of magnitude. The comparisons between the solutions from the implicit high-order GKS on moderate G1 grid and the results from the second-order CFL3D on fine G2 grid in turbulence kinetic energy and specific dissipation rate are given in Figure 4. From Figure 4, even though the implicit high-order GKS is run on moderate G1 grid, the non-dimensional turbulence kinetic energy k and specific dissipation rate ω agree well with the second-order CFL3D on fine grid G2. Quantitative comparisons are as follows. Figure 5(a) shows, for the near wall velocity profile

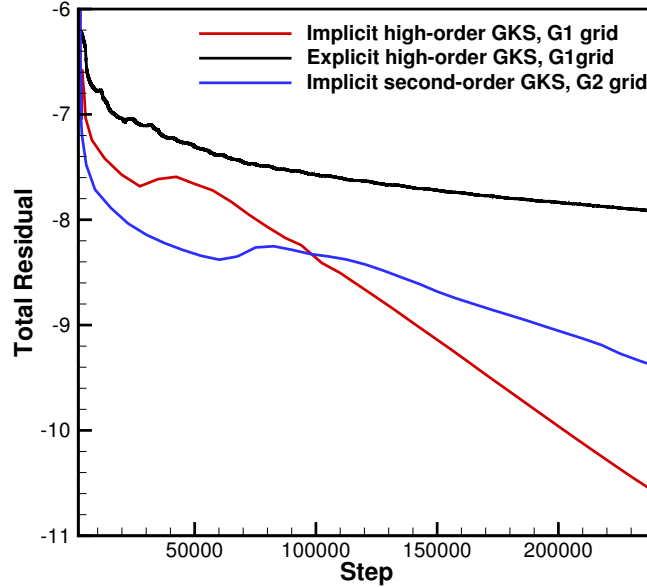


Figure 3: Total residual curves for the implicit/explicit high-order GKS on G1 grid, the implicit second-order GKS on G2 grid.

at $X = 1.9$, the results of implicit high-order GKS on moderate G1 grid is comparable with the second-order GKS/CFL3D on fine G2 grid. For turbulent flow, friction coefficient is very critical in validating the simulation result, as shown in Figure 5(b). The comparable results are shown in Figure 5(b) for frictional coefficient along the flat plate. Specifically, the implicit high-order GKS on moderate G1 grid captures the transition region well, as the transition region from leading edge $x = 0$ to $x = 0.01$ as shown in [20], where the frictional coefficient profile shows a spoon-like curve.

4.4 RANS 3D case: transonic ARA M100 wing-body flow

Transonic flow around three-dimensional complex configuration of ARA M100 wing-body is simulated. This case is adopted to study the robustness of capturing shock and high efficiency in three-dimensional transonic high-Reynolds number flow by the current implicit high-order GKS. Typical cruising condition of ARA M100 is the one corresponding to an angle of attack $\alpha = 2.873^\circ$, Mach number $Ma = 0.8027$, and a root chord based Reynolds number of $Re_{rc} = 1.31 \times 10^7$ (root chord $rc = 0.378\text{m}$). In this paper, C-O type grid of $321 \times 57 \times 49$ provided by [40] is used, with an off wall Y^+ distribution as follows: $Y_{wing}^+ = 0.8$, $0.1 \leq Y_{fuselage}^+ \leq 30$. Configuration of ARA M100 wing-body and surface grid are shown in Figure 6, whose black part is the wing and the green part represents fuselage.

In current study, the total residual reduces down to 4 orders of magnitude. The maximum CFL number of the implicit high-order GKS is 1.8, while the CFL number of the explicit high-order GKS is limited by 0.25. Following analysis is based on the numerical results from the implicit high-order GKS with CFL number 1.

Figure 7 (a) shows pressure coefficient C_p contours on the upper fuselage, where the normal shock footprint on the wing's suction side is observed. To show the shock clearly, Ma contour at $Z/b = 0.935$ near the wing's tip is presented in Figure 7 (b). This wing slice shows the normal shock and its interaction with the turbulent boundary layer, which verify the robustness of the scheme on the capturing of shock.

Comparisons of pressure coefficient C_p profiles at four wing sections among the experimental data, the current implicit high-order GKS, the second-order GKS [18], the second-order Navier-Stokes solver, and results from CFL3D based on S-A model, are plotted in Figure 8. Figure 8 shows that the shock is captured well in all, but the shock of the slices closest to wing root is predicted slightly downstream in comparison

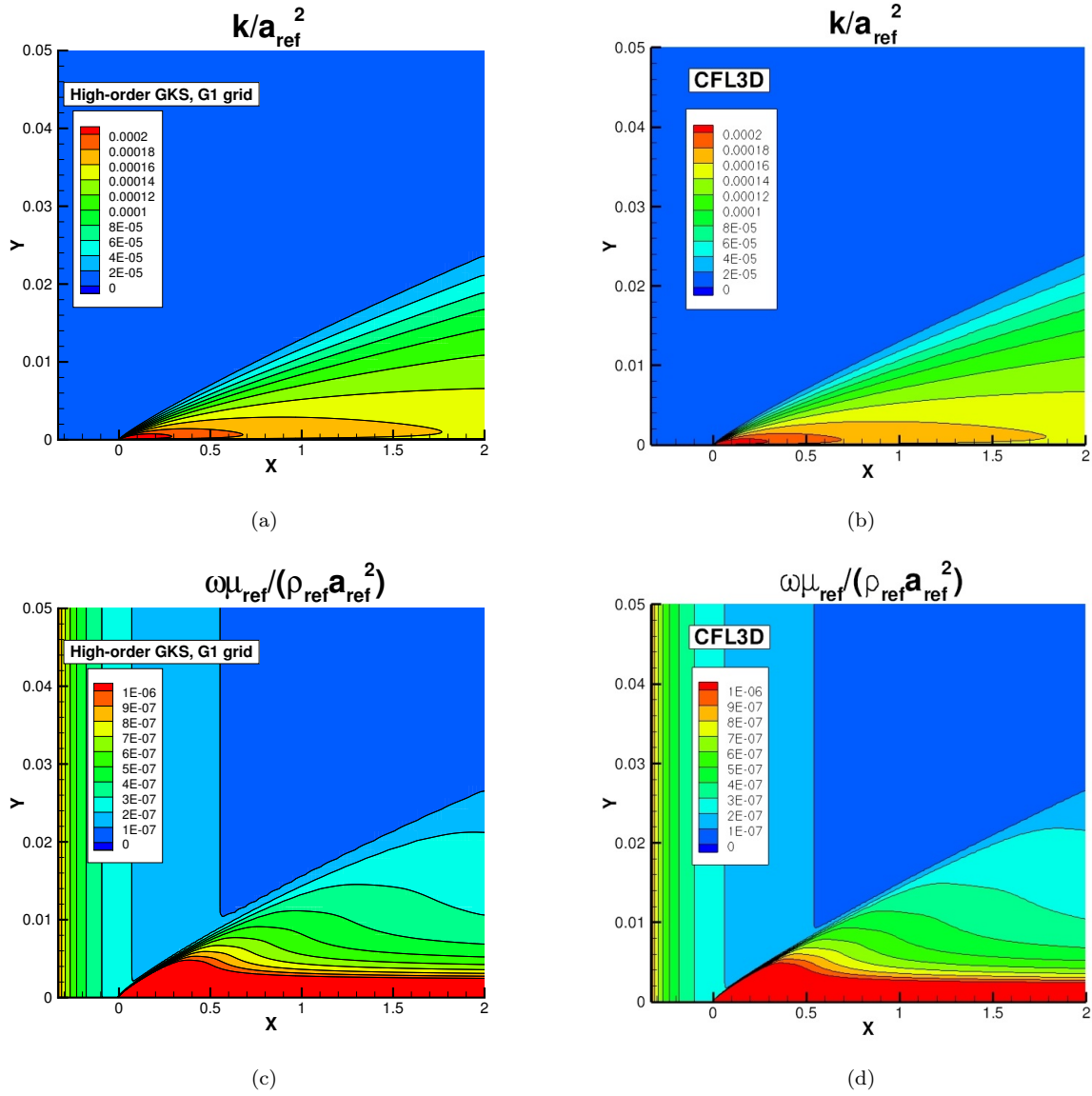


Figure 4: Non-dimensional contours of turbulence kinetic energy k and specific dissipation rate ω , (a)(c) from the high-order GKS on G1 grid, and (b)(d) from the second-order CFL3D on G2 grid.

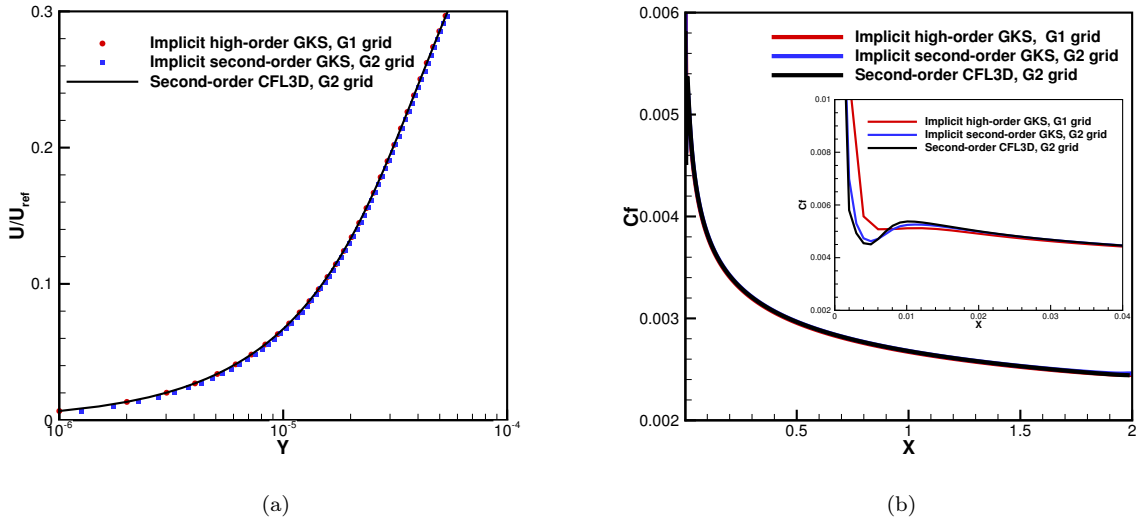


Figure 5: (a) Near wall velocity profile at $x = 1.9$ and (b) frictional coefficient along plate.

with the experiment data. For different turbulence models, numerical results show that $k-\omega$ SST model is a little better than S-A model, which can be seen clearly in Figure 8 (d). In addition, result from GKS coupled with $k-\omega$ SST model outweigh that from Navier-Stokes solver. Compared with the obvious difference between different turbulence model, the current implicit high-order GKS almost takes no advantage than the implicit second-order GKS. It is not surprising as the turbulence model error dominates in this transonic three-dimensional complex RANS simulation rather than the numerical discretization error. This indicates that developing appropriate turbulence model is still the most important task for three-dimensional complex RANS simulation. For transition flows [41, 42, 43], the turbulent model may play an even more important role.

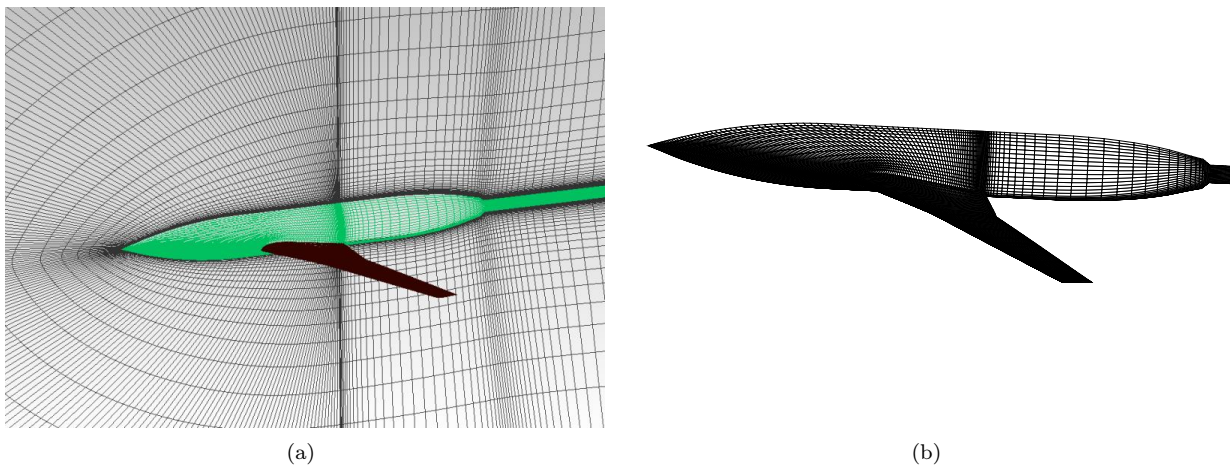


Figure 6: Configuration of ARA M100 wing-body (a) and illustration of surface grid (b).

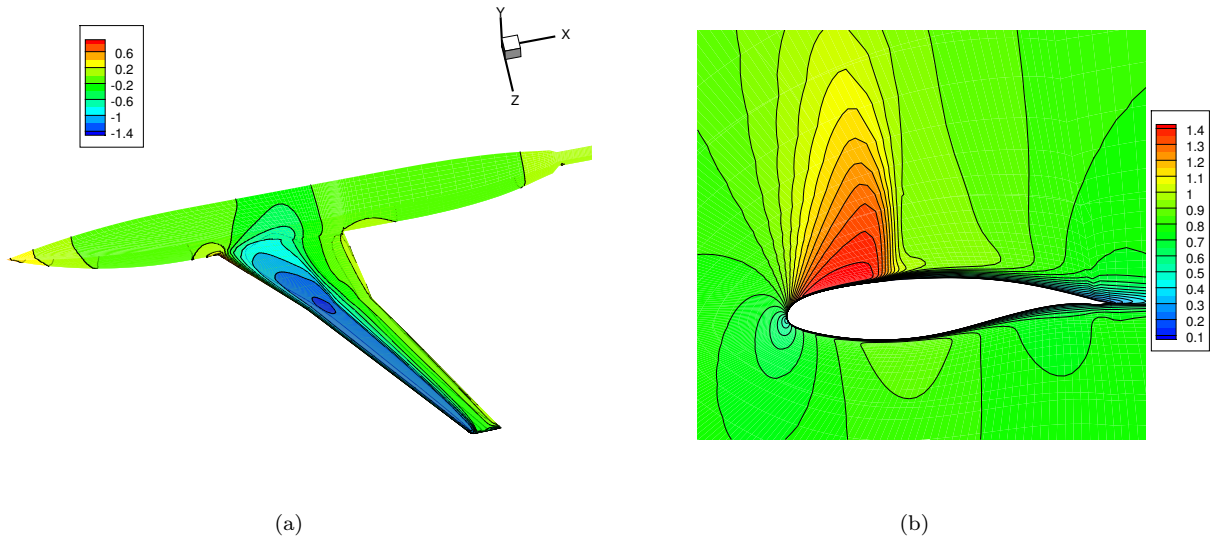


Figure 7: Pressure coefficient C_p contour on the upper fuselage and wing surface (a) Ma contour $Z/b = 0.935$ (b). Z is the distance to the root chord plane and b is the wing span.

5 Conclusion

In present work, targeting on accurate and efficient simulation of three-dimensional turbulent flows, an implicit high-order GKS with LU-SGS method is developed under the two-stage fourth-order framework. Vreman-type LES model for large eddy simulation and $k - \omega$ SST model for RANS simulation are coupled with the current implicit high-order GKS. The cases of Taylor-Green vortex problem, incompressible decaying homogeneous isotropic turbulence, incompressible high-Reynolds number flat plate turbulent flow, and transonic high-Reynolds number ARA M100 wing-body flow, are tested. The high-order GKS shows the higher accuracy in space and time than that of the second-order GKS. Compared with the explicit high-order GKS, the implicit high-order scheme provides great improvement on the computational efficiency. In addition, the robustness of the current implicit high-order GKS and the ability to capture shock are validated in the transonic three-dimensional complex RANS simulation. This transonic 3D simulation indicates that turbulence model plays a leading role in the capturing of high-Reynolds number turbulent flow. Developing appropriate turbulence model is still the most important task for three-dimensional turbulence simulation. The implicit high-order GKS with hybrid RANS/LES model will be studied in the future.

Acknowledgement

Special thanks to Hualin Liu, in College of Aeronautics and Astronautics, Zhejiang University, who provide the helpful discussion and suggestions. The authors would like to thank TianHe-II in Guangzhou, providing high performance computational resources. The current research was supported by Hong Kong research grant council (16206617, 16207715) and National Science Foundation of China (91530319, 11772281).

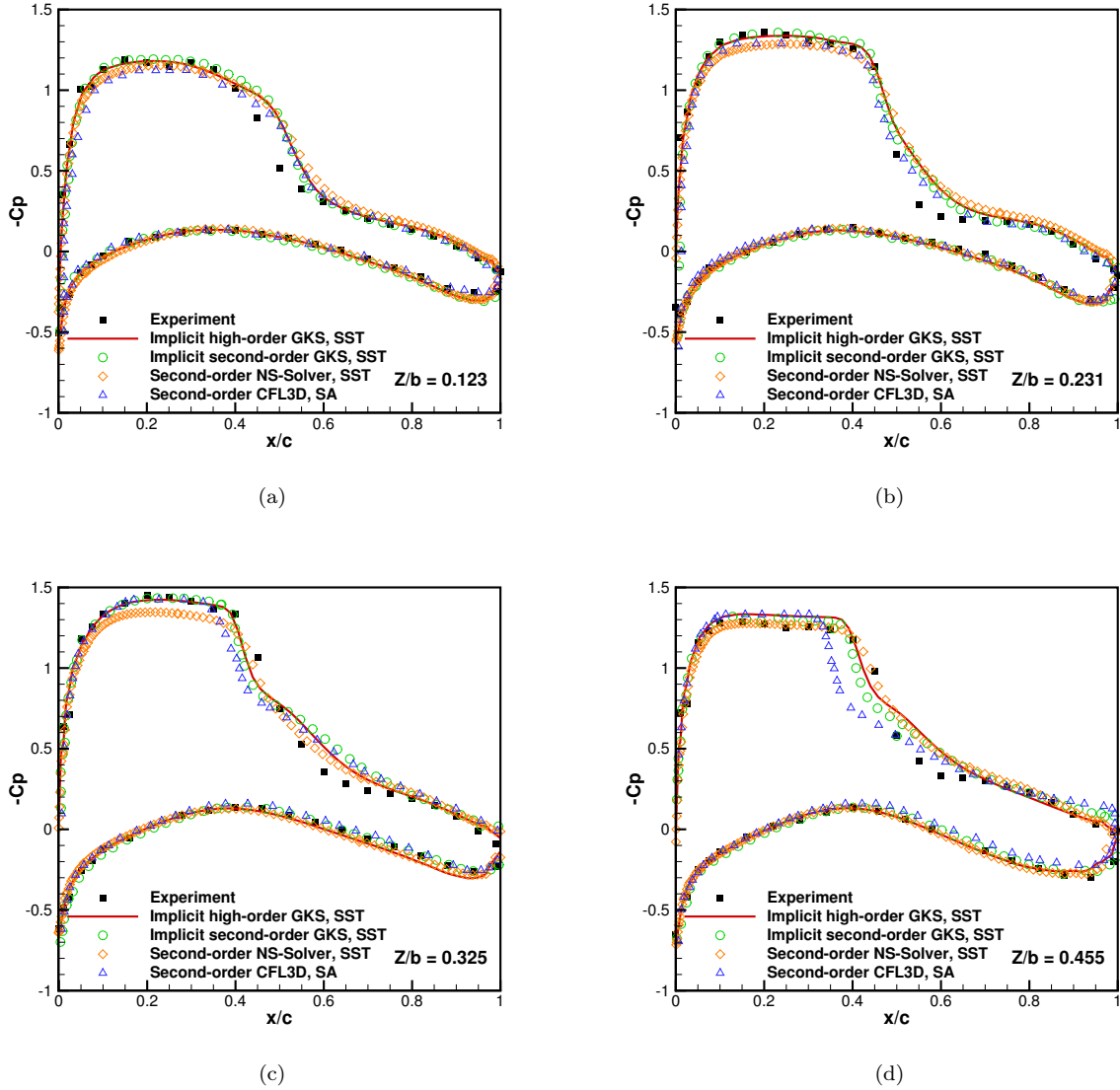


Figure 8: Comparisons of pressure coefficient C_p profiles at selected span-wise locations of ARA M100 wing-body from experiment data, the current implicit high-order GKS, the second-order GKS, the second-order Navier-Stokes solver, and the second-order CFL3D. c is the local chord length.

References

- [1] Hendrik Tennekes and John Leask Lumley. *A first course in turbulence*. MIT press, 1972.
- [2] Stephen B Pope. *Turbulent flows*, 2001.
- [3] David C Wilcox. *Turbulence modeling for CFD*, volume 2. DCW industries La Canada, CA, 1993.
- [4] Pierre Sagaut. *Large eddy simulation for incompressible flows: an introduction*. Springer Science & Business Media, 2006.
- [5] Philippe R Spalart. Detached-eddy simulation. *Annual review of fluid mechanics*, 41:181–202, 2009.
- [6] Pierre Sagaut. *Multiscale and multiresolution approaches in turbulence: LES, DES and hybrid RANS/LES methods: applications and guidelines*. World Scientific, 2013.
- [7] Kun Xu. A gas-kinetic bkg scheme for the navier–stokes equations and its connection with artificial dissipation and godunov method. *Journal of Computational Physics*, 171(1):289–335, 2001.
- [8] Xu Kun. *Direct modeling for computational fluid dynamics: construction and application of unified gas-kinetic schemes*, volume 4. World Scientific, 2014.
- [9] Prabhu Lal Bhatnagar, Eugene P Gross, and Max Krook. A model for collision processes in gases. i. small amplitude processes in charged and neutral one-component systems. *Physical review*, 94(3):511, 1954.
- [10] Kun Xu, Xin He, and Chunpei Cai. Multiple temperature kinetic model and gas-kinetic method for hypersonic non-equilibrium flow computations. *Journal of computational physics*, 227(14):6779–6794, 2008.
- [11] CT Tian, Kun Xu, KL Chan, and LC Deng. A three-dimensional multidimensional gas-kinetic scheme for the navier–stokes equations under gravitational fields. *Journal of Computational Physics*, 226(2):2003–2027, 2007.
- [12] Huazhong Tang, Kun Xu, and Chunpei Cai. Gas-kinetic bkg scheme for three dimensional magnetohydrodynamics. *Numer. Math.: Theory Meth. Appl*, 3(4):387–404, 2010.
- [13] Song Fu and Qibing Li. Numerical simulation of compressible mixing layers. *International journal of heat and fluid flow*, 27(5):895–901, 2006.
- [14] G Kumar, Sharath S Girimaji, and J Kerimo. Weno-enhanced gas-kinetic scheme for direct simulations of compressible transition and turbulence. *Journal of Computational Physics*, 234:499–523, 2013.
- [15] Hudong Chen, Satheesh Kandasamy, Steven Orszag, Rick Shock, Sauro Succi, and Victor Yakhot. Extended boltzmann kinetic equation for turbulent flows. *Science*, 301(5633):633–636, 2003.
- [16] Hudong Chen, Steven A Orszag, Ilya Staroselsky, and Sauro Succi. Expanded analogy between boltzmann kinetic theory of fluids and turbulence. *Journal of Fluid Mechanics*, 519:301–314, 2004.
- [17] Dongxin Pan, Chengwen Zhong, Ji Li, and Congshan Zhuo. A gas-kinetic scheme for the simulation of turbulent flows on unstructured meshes. *International Journal for Numerical Methods in Fluids*, 82(11):748–769, 2016.
- [18] Jin Jiang and Yuehong Qian. Implicit gas-kinetic bkg scheme with multigrid for 3d stationary transonic high-reynolds number flows. *Computers & Fluids*, 66:21–28, 2012.
- [19] Marcello Righi. A gas-kinetic scheme for turbulent flow. *Flow, Turbulence and Combustion*, 97(1):121–139, 2016.
- [20] Ji Li, Chengwen Zhong, Dongxin Pan, and Congshan Zhuo. A gas-kinetic scheme coupled with sst model for turbulent flows. *Computers & Mathematics with Applications*, 2016.
- [21] Shuang Tan, Qibing Li, Zhixiang Xiao, and Song Fu. Gas kinetic scheme for turbulence simulation. *Aerospace Science and Technology*, 78:214–227, 2018.
- [22] Jiequan Li and Zhifang Du. A two-stage fourth order time-accurate discretization for lax–wendroff type flow solvers i. hyperbolic conservation laws. *SIAM Journal on Scientific Computing*, 38(5):A3046–A3069, 2016.
- [23] Liang Pan, Kun Xu, Qibing Li, and Jiequan Li. An efficient and accurate two-stage fourth-order gas-kinetic scheme for the euler and navier–stokes equations. *Journal of Computational Physics*, 326:197–221, 2016.
- [24] Xing Ji, Fengxiang Zhao, Wei Shyy, and Kun Xu. A family of high-order gas-kinetic schemes and its comparison with riemann solver based high-order methods. *Journal of Computational Physics*, 356:150–173, 2018.
- [25] Seokkwan Yoon and Antony Jameson. An LU-SSOR scheme for the Euler and Navier-Stokes equations.

- NASA CR-179556,AIAA-87-0600, 1986.
- [26] G Barakos and D Drikakis. Implicit unfactored implementation of two-equation turbulence models in compressible navier-stokes methods. *International journal for numerical methods in fluids*, 28(1):73–94, 1998.
 - [27] AW Vreman. An eddy-viscosity subgrid-scale model for turbulent shear flow: Algebraic theory and applications. *Physics of fluids*, 16(10):3670–3681, 2004.
 - [28] Florian R Menter. Two-equation eddy-viscosity turbulence models for engineering applications. *AIAA journal*, 32(8):1598–1605, 1994.
 - [29] Sydney Chapman and TG Cowling. The mathematical theory of non-uniform gases: An account of the kinetic theory of viscosity, thermal conduction and diffusion in gases. cambridge mathematical library. *Cambridge University Press*, 1:27–52, 1970.
 - [30] Taku Ohwada and Kun Xu. The kinetic scheme for the full-burnett equations. *Journal of computational physics*, 201(1):315–332, 2004.
 - [31] Guang-Shan Jiang and Chi-Wang Shu. Efficient implementation of weighted eno schemes. *Journal of computational physics*, 126(1):202–228, 1996.
 - [32] Qibing Li, Kun Xu, and Song Fu. A high-order gas-kinetic navier–stokes flow solver. *Journal of Computational Physics*, 229(19):6715–6731, 2010.
 - [33] Xiaodong Ren, Kun Xu, Wei Shyy, and Chunwei Gu. A multi-dimensional high-order discontinuous galerkin method based on gas kinetic theory for viscous flow computations. *Journal of Computational Physics*, 292:176–193, 2015.
 - [34] Liang Pan and Kun Xu. A third-order compact gas-kinetic scheme on unstructured meshes for compressible navier–stokes solutions. *Journal of Computational Physics*, 318:327–348, 2016.
 - [35] Kun Xu, Meiliang Mao, and Lei Tang. A multidimensional gas-kinetic bgk scheme for hypersonic viscous flow. *Journal of Computational Physics*, 203(2):405–421, 2005.
 - [36] Qibing Li and Song Fu. Applications of implicit bgk scheme in near-continuum flow. *International Journal of Computational Fluid Dynamics*, 20(6):453–461, 2006.
 - [37] James DeBonis. Solutions of the taylor-green vortex problem using high-resolution explicit finite difference methods. In *51st AIAA Aerospace Sciences Meeting including the New Horizons Forum and Aerospace Exposition*, page 382, 2013.
 - [38] Genevieve Comte-Bellot and Stanley Corrsin. Simple eulerian time correlation of full-and narrow-band velocity signals in grid-generated, isotropic turbulence. *Journal of Fluid Mechanics*, 48(2):273–337, 1971.
 - [39] Turbulence modeling resource. <<https://turbmodels.larc.nasa.gov/>>.
 - [40] CFL3D Version 6 home page. <<http://cfl3d.larc.nasa.gov/>>.
 - [41] CB Lee. Possible universal transitional scenario in a flat plate boundary layer: Measurement and visualization. *Physical Review E*, 62(3):3659, 2000.
 - [42] CB Lee and S Fu. On the formation of the chain of ring-like vortices in a transitional boundary layer. *Experiments in fluids*, 30(3):354–357, 2001.
 - [43] CB Lee and JZ Wu. Transition in wall-bounded flows. *Applied Mechanics Reviews*, 61(3):030802, 2008.